



HAL
open science

Room Temperature-Integrated Photodetector between 5 μm and 8 μm Wavelength

Thi Hao Nhi Nguyen, Natnicha Koopai, Victor Turpaud, Miguel Montesinos-Ballester, Jacopo Frigerio, Stefano Calcaterra, Andrea Ballabio, Xavier Le Roux, Jean- René Coudevylle, Cédric Villebasse, et al.

► To cite this version:

Thi Hao Nhi Nguyen, Natnicha Koopai, Victor Turpaud, Miguel Montesinos-Ballester, Jacopo Frigerio, et al.. Room Temperature-Integrated Photodetector between 5 μm and 8 μm Wavelength. *Advanced Photonics Research*, 2023, 4 (2), pp.2200237. 10.1002/adpr.202200237 . hal-04077500

HAL Id: hal-04077500

<https://hal.science/hal-04077500>

Submitted on 21 Apr 2023

HAL is a multi-disciplinary open access archive for the deposit and dissemination of scientific research documents, whether they are published or not. The documents may come from teaching and research institutions in France or abroad, or from public or private research centers.

L'archive ouverte pluridisciplinaire **HAL**, est destinée au dépôt et à la diffusion de documents scientifiques de niveau recherche, publiés ou non, émanant des établissements d'enseignement et de recherche français ou étrangers, des laboratoires publics ou privés.

Room Temperature-Integrated Photodetector between 5 μm and 8 μm Wavelength

Thi Hao Nhi Nguyen, Natnicha Koopai, Victor Turpaud, Miguel Montesinos-Ballester, Jacopo Frigerio, Stefano Calcaterra, Andrea Ballabio, Xavier Le Roux, Jean-René Coudevylle, Cédric Villebasse, David Bouville, Carlos Alonso-Ramos, Laurent Vivien, Giovanni Isella, and Delphine Marris-Morini*

Mid-infrared (mid-IR) optics has a great importance for a large number of applications in sensing, imaging, or even telecommunication. However, high-speed and room-temperature-integrated photodetector (PD) operating in a wide spectrum of the mid-IR is a critical device that is currently missing for the development of compact and efficient spectroscopic systems exploiting synchronous detection. Herein, a waveguide-integrated PD based on a Schottky diode embedded in a graded silicon germanium waveguide is demonstrated. Photodetection is obtained in a wide spectral range from 5 to 8 μm wavelength, with responsivity reaching up to 0.1 mA W^{-1} . Photodetection performed in pulsed regime with laser pulse width between 50 and 200 ns indicates an operation beyond 20 MHz. Interestingly, the achieved performances indicate that this device is already suitable for on-chip signal monitoring, while further improvement can pave the way toward advanced compact and fully integrated spectroscopic systems operating in long-wave infrared regions.

1. Introduction

Spectroscopy in the mid-infrared (mid-IR) wavelength range (from 2 to 20 μm wavelength) is an important technique to detect and identify chemical and biological substances due to the strong vibrational and rotational resonances leading to light absorption at specific wavelengths in the mid-IR. This so-called molecular fingerprint region can, hence, be exploited to detect small traces of hazardous and toxic substances in a large variety of applications including environmental monitoring, hazard detection, industrial process control, or medical diagnosis.^[1–3] A challenging task is to make mid-IR spectroscopy accessible in remote areas, driving the development of compact and cost-effective solutions to replace table-top systems.

The development of mid-IR photonic circuits that integrate complete optical functions has witnessed a burst of research activity in the recent years. Different solutions have been explored for the development of an integrated mid-IR sensing platform, based on chalcogenide glasses,^[4–6] quantum cascade lasers (QCL),^[7,8] or silicon (Si) photonics.^[9–12] Among them, mid-IR Si photonics present the advantage of leveraging on the high-volume fabrication technologies already developed for microelectronic integrated circuits to provide reliable and cost-efficient solutions. In this context, graded silicon germanium (SiGe) photonics circuits have shown to be a good candidate for the development of a mid-IR photonic platform. Indeed, it has been shown that graded SiGe waveguides can be used with low propagation losses in an unprecedented spectral range (reported from 5 to 11 μm wavelengths) and for both transverse electric (TE) and transverse magnetic (TM) polarizations.^[13] Furthermore, the ability to fine-tune the light confinement and the waveguide dispersion, together with the strong Kerr effect of Ge and Ge-rich alloys, allowed the demonstration of ultra wideband-integrated light source based on supercontinuum generation.^[14] As a next step to achieve a complete mid-IR photonic platform, active devices are required. While electrically driven integrated optical modulator has been demonstrated recently,^[3] this work reports the first integrated photodetector (PD) operating at room temperature in a wide range in the mid-IR, from 5 to 8 μm wavelength.

T. H. N. Nguyen, N. Koopai, V. Turpaud, M. Montesinos-Ballester,^[†] X. Le Roux, J. R. Coudevylle, C. Villebasse, D. Bouville, C. Alonso-Ramos, L. Vivien, D. Marris-Morini

Centre de Nanosciences et de Nanotechnologies
CNRS


Université Paris-Saclay
91120 Palaiseau, France

E-mail: delphine.morini@universite-paris-saclay.fr

J. Frigerio, S. Calcaterra, A. Ballabio, G. Isella
L-NESS

Dipartimento di Fisica
Politecnico di Milano

Polo di Como, Via Anzani 42, 22100 Como, Italy

 The ORCID identification number(s) for the author(s) of this article can be found under <https://doi.org/10.1002/adpr.202200237>.

^[†]Present address: Institute for Quantum Electronics, ETH Zurich, Zurich 8093, Switzerland

© 2022 The Authors. Advanced Photonics Research published by Wiley-VCH GmbH. This is an open access article under the terms of the Creative Commons Attribution License, which permits use, distribution and reproduction in any medium, provided the original work is properly cited.

DOI: 10.1002/adpr.202200237

Different physical mechanisms are currently used for mid-IR photodetection. While thermal detectors exploiting microbolometers can be used to detect mid-IR signals in a wide spectral range, quantum detectors feature higher sensitivity, and speed. In the deep mid-IR spectrum ($\lambda > 6 \mu\text{m}$), interband transitions can be exploited in narrow bandgap materials such as mercury cadmium telluride (HgCdTe)^[15] or lead telluride (PbTe),^[16] while intersubband transitions can be exploited in III–V multiquantum well heterostructures.^[17–19]

In this work, we show that it is possible to detect mid-IR signal directly within the SiGe waveguide, at room temperature, by mean of an embedded Schottky diode to collect the generated photocurrent. A maximum responsivity up to 0.1 mA W^{-1} is obtained. Furthermore, pulsed operation is also demonstrated, with pulse widths as small as 50 ns (limited by the experimental set-up), which paves the way toward advanced applications requiring high-speed operation.

2. Results and Discussion

2.1. Photodetector Design and Fabrication

The integrated PD is based on a $6 \mu\text{m}$ -thick-graded SiGe waveguide, in which the refractive index increases linearly along the vertical direction, grown on an n-doped Si substrate. The waveguide width is $6 \mu\text{m}$, and the etching depth is $5.5 \mu\text{m}$, as depicted in Figure 1a. The top electrical contact exploits a coplanar waveguide (CPW) structure on top of the waveguide, while a

bottom electrical contact at the backside of the device is connected to the ground pad. Thus, a vertical diode is obtained, as the top contact is expected to feature a Schottky behavior, while the bottom contact on highly n-doped Si is expected to be ohmic.^[3] The electrodes have been designed to ensure a characteristic impedance of the line around 50Ω with a reduced radio frequency (RF) propagation loss. The main parameters for the optimization are the width of the signal line path and the gap between the signal and ground pads. The presence of the photodiode has a major influence in the RF characteristics of the line. Thus, the equivalent electrical circuit of the Schottky diode is inserted in the calculation. It consists in a capacitance (estimated from C–V characterization) in series with the access resistance (estimated from I–V characterization). The impedance and electrical transmission of the line have then been calculated and compared for different values of the design parameters. After optimization, the metallic signal line width is chosen to be $4 \mu\text{m}$, while the gap between signal and ground pads is $10 \mu\text{m}$. Since the TM polarization suffers from high loss due to the presence of the metal on top of the waveguide, only the TE polarization is considered in the following. A numerical simulation of the optical mode at the wavelength of $6.4 \mu\text{m}$ is reported in Figure 1b. The complete photonic circuit including the mid-IR diode-based PD is shown in the schematic of Figure 1c. The input light is coupled to the photonic circuit through a $15 \mu\text{m}$ -wide input waveguide. The waveguide width is then reduced to $6 \mu\text{m}$ by a $200 \mu\text{m}$ -long taper. The core of the PD is a $500 \mu\text{m}$ -long waveguide. Multimode interferometer

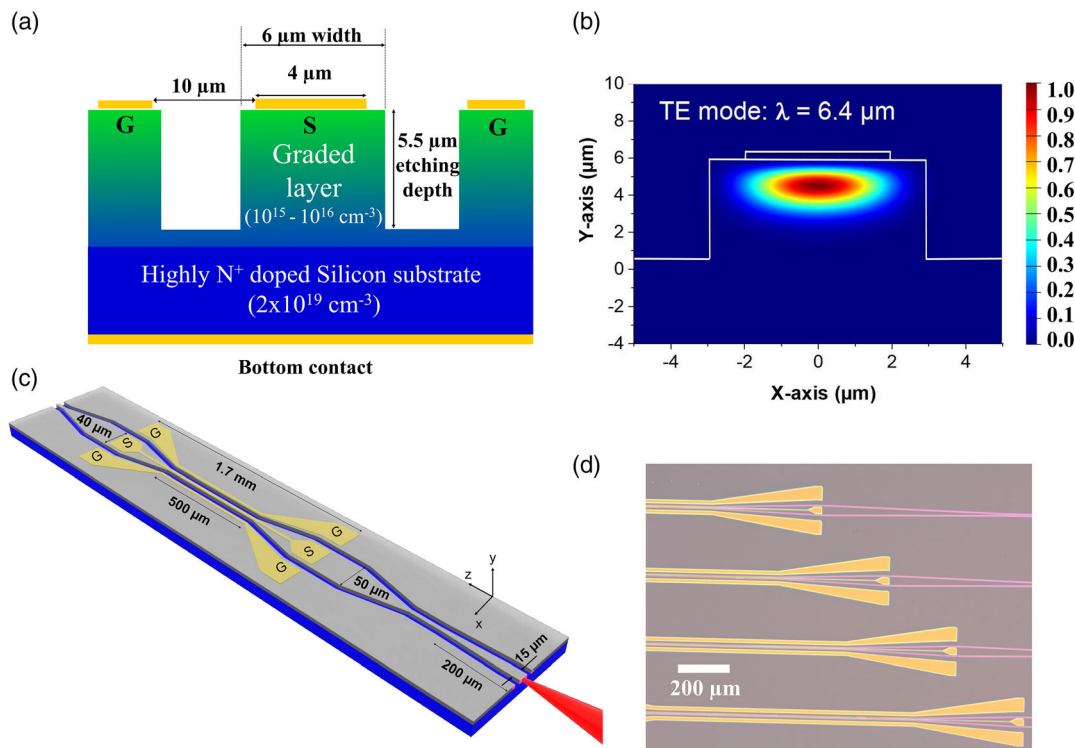


Figure 1. Device design. a) Schematic cut-view of the active region of the photodetector. b) Optical simulation of the fundamental TE mode at the wavelength of $6.4 \mu\text{m}$. Scale bar: Relative optical intensity. c) Schematic top view of the photonic circuit including the integrated photodetector. The CPW electrodes on the top can be seen. d) Optical microscope picture of the fabricated device.

couplers (MMI) are used at its input and output, to enlarge the width of the waveguide up to 50 μm , which enables access to the CPW electrodes with RF electrical probes. The choice of an MMI to enlarge the waveguide build on previous demonstration of broadband mid-IR MMI in graded SiGe waveguide.^[20] In this work, a 1×1 MMI coupler has been then optimized to achieve 50 μm wide waveguide and broadband operation is obtained from 5 μm to 8 μm wavelength, with loss estimated from 1 to 1.6 dB (Figure S1, Supporting Information). When considering the total length between both ground-signal-ground (GSG) contact pads, the integrated waveguide PD is 1.7 mm long.

In terms of fabrication, the SiGe growth is performed by low energy plasma-enhanced chemical vapor deposition (LEPECVD) on top of a highly n-type doped Si substrate (doping concentration of $2 \times 10^{19} \text{ cm}^{-3}$). The structures are then patterned using electron-beam lithography and dry etching steps. The top contact is defined by lift-off, while the bottom contact is deposited on the whole backside surface. Both contacts are made of 10 nm thick of titanium (Ti) and 300 nm of gold (Au). An optical microscope picture of the final device can be seen in Figure 1d.

2.2. Electrical Characterization

Current–voltage (I – V) and capacitance–voltage (C – V) measurements have been performed to investigate the electrical behavior of the device. All the measurements are carried out at room temperature. I – V characterization of the 1.7 mm-long diode is reported in Figure 2a, showing a good rectifying behavior, which is explained by the presence of a Schottky barrier at the top contact, while the bottom contact on highly N+ doped substrate is ohmic. From this measurement, a Schottky barrier height of 0.58 eV can be deduced, with an ideality factor of 1.44, which is close to similar devices exploiting the same epitaxial growth.^[3] From the derivative of the I – V curve in the injection regime, it is possible to estimate a serial resistance of 2.5 Ω for the 1.7 mm-long diode.

When operating in depletion regime, the electric field in the depleted region of the diode (space charge region) can be used to extract the photogenerated carrier and to create the photocurrent. C – V measurements have been used to characterize the space

charge region below the top contact. The C – V measurements have been done on dedicated squared mesas fabricated on the same photonic circuit, and the results are reported in Figure 2b. The capacitance varies linearly with the mesa surface. Furthermore, as expected, the device capacitance decreases when the reverse voltage increases, which is explained by the increase of the depleted region when the reverse voltage increases, as depicted in Figure 3. The doping concentration in the graded layer can be extracted by fitting the measured capacitance with numerical simulations. The comparison between measurement and simulation of $1/C^2$ is shown in Figure 2c, and the doping concentration is estimated to be of $1.5\text{--}2 \times 10^{15} \text{ cm}^{-3}$ (N-doped) in the SiGe epitaxial layer.

2.3. Electro-Optical Characterization

To evaluate the electro-optical response of the device, light coming from a tunable external cavity based QCL is coupled in the photonic circuit, using an aspheric ZnSe lens. In the first measurement, the QCL operates in pulsed mode with a repetition rate of 100 kHz and a duty cycle of 5%. The I – V characteristics are then measured in depletion regime, both at dark and under illumination conditions, and for different input wavelengths. For example, a measurement at 5.5 μm wavelength is shown in Figure 4. For this specific wavelength, the mean value of the optical power coupled in the PD is estimated to be 2.7 mW. The measurement is performed at room temperature, and the temperature of the photonic circuit is not controlled. Interestingly, a clear photocurrent can be seen above the dark current level, while the photon energy is well below the bandgap energy of the SiGe alloy.

The PD sensitivity has been quantified by estimating the external and internal responsivity, defined hereafter. The external responsivity is defined as $R_{\text{ext}} = I_{\text{ph}}/P_{\text{QCL}}$, where I_{ph} is the collected photocurrent and P_{QCL} is the optical input power measured using a power meter at the output of the QCL source, before the lens used to couple the light into the photonic circuit. The internal responsivity is defined as $R_{\text{int}} = I_{\text{ph}}/P_{\text{coupled}}$, where P_{coupled} is the power coupled in the photonic circuit, at the input of the PD. P_{coupled} is estimated by considering (i) the

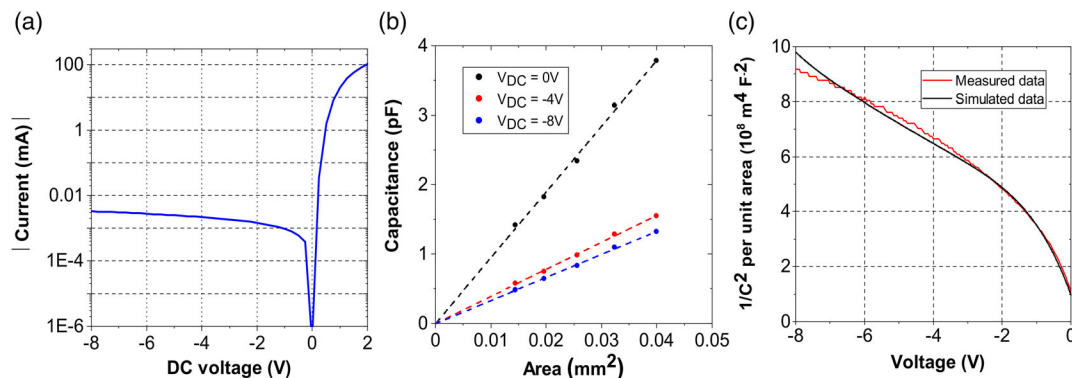


Figure 2. Electrical characterization of the photodetector. a) Current/voltage characteristics in the dark regime. b) Measured capacitance as a function of the device areas, for different reverse bias voltages. c) Comparison between measured and the simulated results of $1/C^2$ as a function of reverse bias voltages. In the simulation, the residual doping in the SiGe epilayer is n-type, with a concentration of $1.5 \times 10^{15} \text{ cm}^{-3}$ from the top of waveguide to 2.5 μm depth and $2 \times 10^{15} \text{ cm}^{-3}$ down to the 6 μm depth.

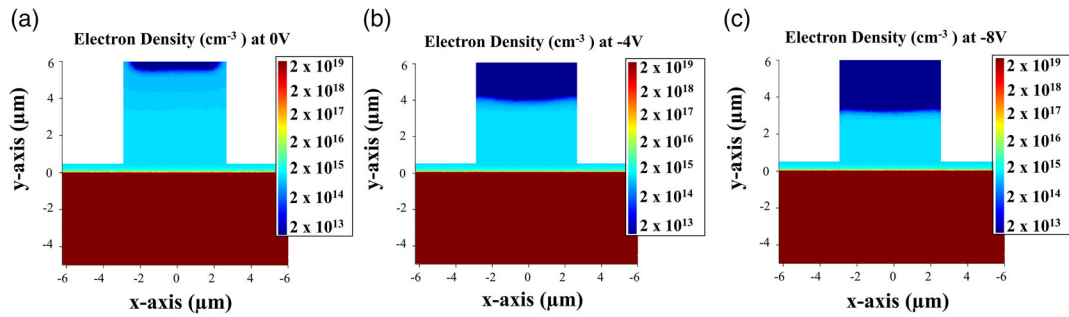


Figure 3. Electrical simulations of the photodiode. a–c) Free electron concentration in the integrated photodetector with reverse bias voltages of 0, –4, and –8 V, respectively. The extension of the space charge region below the top contact is clearly seen when the reverse voltage is increased. The residual doping concentration in the SiGe epilayer is n-type, with a value of $1.5 \times 10^{15} \text{ cm}^{-3}$ from the top of the waveguide to 2.5 μm depth and with $2 \times 10^{15} \text{ cm}^{-3}$ down to the 6 μm depth. The Si substrate is n-type, with a doping concentration of $2 \times 10^{19} \text{ cm}^{-3}$.

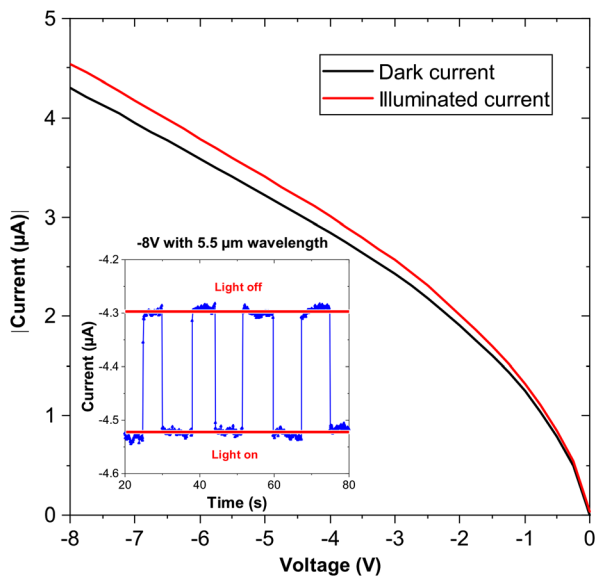


Figure 4. I – V characterization of photodetector. I – V curves in both dark and illuminated conditions at 5.5 μm wavelength. Inset: the experimental variation of the current at –8 V reverse bias voltage when the mid-IR light is turned on and off.

butt-coupling efficiency, (ii) the propagation loss in the 1 cm-long input waveguide before the PD entrance, and (iii) the loss of the MMI. The contribution of butt coupling and MMI coupler has been numerically evaluated and is assumed to be 6.5 dB from 5 to 8 μm wavelength (Figure S1, Supporting Information). The waveguide propagation loss has been experimentally determined by means of the cut-back method in a separate chip and varies from 1 to 4 dB cm^{-1} as a function of the wavelength (Figure S2, Supporting Information).

Both the external and internal responsivities are reported in Figure 5. Interestingly, the photogenerated current and so the responsivity increases when the reverse bias applied voltage is increased, as reported in Figure 5a for the wavelengths of 5.5 and 6.4 μm . Furthermore, a clear photoresponse is obtained from 5 to 8 μm at the bias voltage of –8 V (Figure 5b). Finally, when considering the light effectively coupled in the PD, an internal

responsivity up to 0.1 mA W^{-1} is obtained at 5.2 μm (Figure 5c). It should be noted that wavelength below 5.2 μm cannot be reached with the laser used in the experimental set-up. From these measurements, the noise equivalence power (NEP), referred as the light intensity below which the photogenerated current becomes indistinguishable from dark current,^[21] is determined to be $1.3 \times 10^{-8} \text{ W}/\sqrt{\text{Hz}}$ and $1.6 \times 10^{-8} \text{ W}/\sqrt{\text{Hz}}$ at –8 and –4 V bias voltages at the wavelength of 5.5 μm , respectively.

The evaluation of the PD electro-optical bandwidth is challenging because of the lack of efficient and high-speed modulators in this wavelength range. In order to estimate the device speed, the pulsed operation of a QCL operating at a repetition rate of 1 MHz is exploited, with tunable duty cycle from 5 to 20%. However, in this configuration, the amplitude of the photocurrent is limited around 0.2 μA , which prevents the possibility to directly measure the time evolution of the signal on an oscilloscope. The mean value of the generated photocurrent has thus been measured for different pulse widths from 50 to 200 ns. If the photocurrent would be generated with a time constant much larger than the pulse width, it would not reach its maximum value during the pulse duration, thus a reduction on the measured mean value of the photocurrent would be obtained. Even if this is not a direct measurement of the photocurrent at high frequency, it is believed that any drastic limitation of the PD bandwidth would imply a reduction of the responsivity when a short pulse-input light is used. Furthermore, as the device speed is expected to be independent from the wavelength, the measurement is done at the 7.8 μm wavelength corresponding to the maximum output power of the QCL.

Figure 6 reports the measured external and internal responsivity for different values of the QCL pulse width, at the wavelength of 7.8 μm and for –8 V applied voltage. The difference between the 2 curves is due to the total contributed losses (coupling loss and propagation loss before the PD). Noticeably, the measured responsivities do not crucially depend on the QCL pulse width, down to pulse width as small as 50 ns (limited by the QCL used in the experiment). This indicates that the device electro-optical bandwidth is expected to be larger than 20 MHz, which is more than enough for synchronous detection experiment.

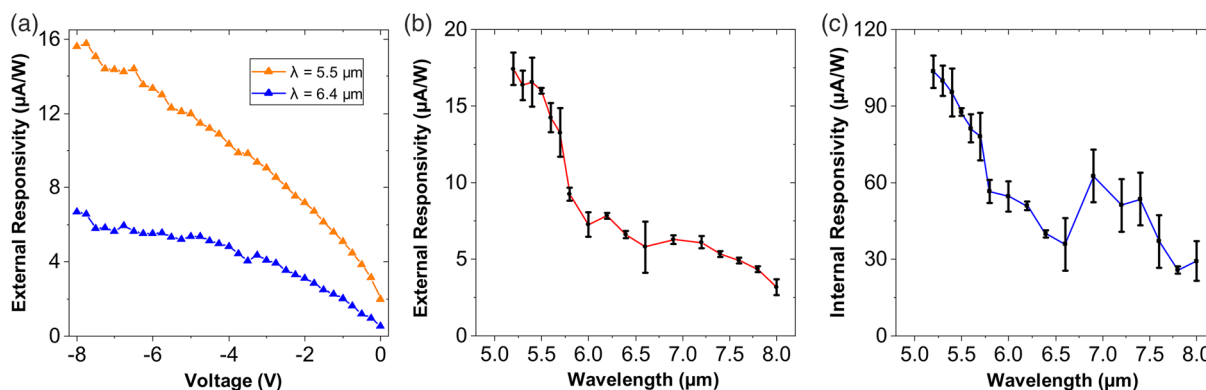


Figure 5. Responsivity characterization. a) External responsivity as a function of the reverse bias voltage at two specific wavelengths of 5.5 μm (orange line) and 6.4 μm (blue line). b, c) External and internal responsivity of the photodetector as a function of the mid-IR wavelength with -8 V applied to the device, respectively.

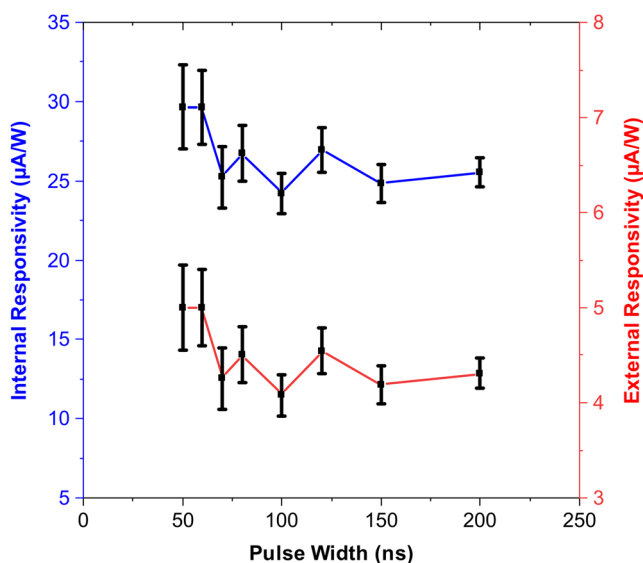


Figure 6. Device speed characterization. External (red solid line) and internal (blue solid line) responsivity of the photodetector as a function of pulsed width at the wavelength of 7.8 μm with -8 V applied to the structure.

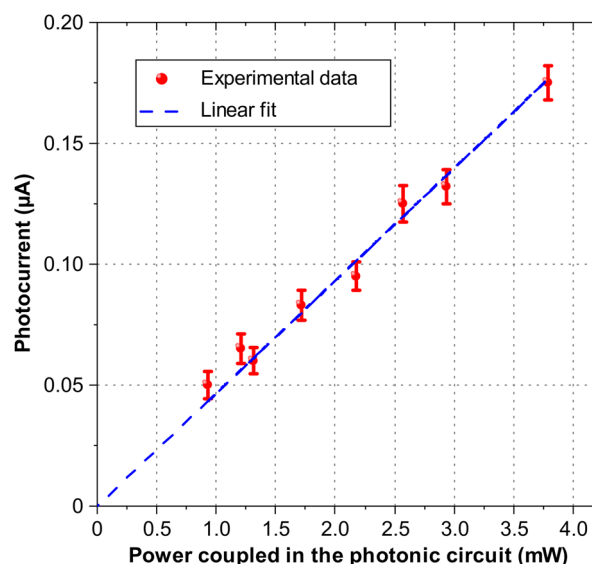


Figure 7. Photocurrent response. Measured photocurrent as function of the power coupled in the photonic circuit, at the photodetector input, at the wavelength of 7.8 μm.

By changing the pulse width of the QCL, the optical power at the output of the QCL source is also varied; therefore, these measurements also allow to investigate the linearity of the PD. The measured photocurrent as a function of the power coupled in the photonic circuit is reported in **Figure 7**, where a linear dependence is clearly seen.

3. Analysis

Based on the detailed electro-optical analysis of the PD that has been reported, it is important to identify the mechanism at the origin of the photocurrent. The bandgap energy of SiGe alloys is much higher than the photon energy corresponding to wavelengths longer than 5 μm; therefore, interband absorption cannot

be responsible for the observed photocurrent. Alternative mechanisms thus need to be investigated. When comparing the device structure and the optical field distribution in the waveguide, it can be deduced that the free carriers that are collected by the diode must be created either in the SiGe alloy or in the metallic contact. Mid-IR photodetectors based on surface plasmonic absorption and hot-carrier generation in the interface between a metal and a semiconductor have been demonstrated in the literature for optical wavelengths below 4 μm.^[22–24] However, in the work reported here, the photon energy ranges from 0.15 to 0.25 eV, which is much smaller than the Schottky barrier height of 0.58 eV. Furthermore, no variation of the barrier height could be detected from the analysis of the I - V curves in the injection scheme with and without illumination. An alternative mechanism leading to free carrier generation is related to the energy dissipated by free carrier absorption that could raise the

temperature within the PD. This would increase the intrinsic carrier density giving rise to an illumination-dependent current. This effect is, however, negligibly small in the photodetectors under investigation and must also be disregarded.

Defect-mediated sub-bandgap absorption has been demonstrated previously using silicon-on-insulator (SOI) platform, for wavelengths from 2.2 to 2.4 μm . However, in these works, defects have been introduced on purpose, using ion implantation of the structures.^[25,26] In another study, Brath et al.^[27] have reported that 60° dislocations in mechanically deformed germanium give rise to optical absorption in the 0.1 and 0.2 eV spectral region. In n-type Ge, such relatively broad absorption lines are attributed to transitions promoting electrons from dislocation-related states to the conduction band, a mechanism consistent with the observed photocurrent. The epitaxial growth of SiGe on Si leads to the nucleation of dislocations. In linearly graded buffers, such misfit dislocations^[28] are not confined at the SiGe/Si interface but are homogeneously distributed within the graded region resulting in an effective overlap between the dislocation-related states, the optical mode, and the depleted region. This mechanism could therefore explain the observed electro-optical response.

4. Conclusion

In conclusion, this work reports an on chip-integrated PD operating in a wide spectral range of the mid-IR. The PD operates at room temperature, between 5 and 8 μm wavelength, and shows an internal responsivity up to 0.1 mA W^{-1} . Operation is demonstrated with pulse as short as 50 ns, which is a good indication of high-speed operation, at least up to 20 MHz. Interestingly, with the reported performances, this integrated PD can already have a strong impact for monitoring light on chip, for example, when coupling light from an external QCL to a photonic circuit or in sensing experiments. Further improvements of the device performances will require a deeper understanding of the photocurrent generation mechanism, a better evaluation of the cutoff frequency, and possibly an engineering of the depleted region.

5. Experimental Section

Sample Fabrication: The 6 μm -thick SiGe graded layer is epitaxially grown on the highly n-doped silicon substrate. The residual doping concentration in the graded layer is around 10^{15} – 10^{16} cm^{-3} , while doping concentration of the Si substrate is $2 \times 10^{19} \text{ cm}^{-3}$. This growth process is performed by LEPECVD.^[29] The PD device is fabricated in the cleanroom with two lithography steps. The first e-beam lithography is intended to define the pattern of metal contacts. Then, metal deposition is carried out, which is made of 10 nm titanium (Ti) followed by 300 nm gold (Au), and subsequently the lift-off process. The second lithography step is done in order to pattern the photonic waveguide. ICP-RIE etching is then used to etch the 5.5 μm deep waveguide. Finally, after polishing at the backside of the sample, the same metal stack is deposited on the whole surface of the backside to form the bottom ohmic contact.

Photoresponse Setup: A mid-IR quantum-cascaded laser (MIRCAT, daylight solution) with a pulse rate of 100 kHz and a duty cycle of 5% is used to cover a wide spectral range from 5.2 μm up to 11 μm . The light emitted from the QCL is butt coupled to the photonic chip by ZnSe aspherical lens. The power meter is set in front of input lens to measure the optical input power injected to the photonic circuit P_{QCL} . The sample is stucked to a

metallic holder by means of a conducting glue (indium paste). The RF probe with ground signal (GS) electrodes is in contact with the metallic contact pads on top of the sample. In order to provide the DC voltage to the PD, a source-meter equipment (Keithley 2400) is used and connected with a lock-in detection system by a bias-tee to amplify the signal. High-speed photodetection measurements, which are performed using a different pulsed-wave QCL with higher power at the wavelength of 7.8 μm and different pulse widths (50–200 ns) and pulse rates (100 kHz–2 MHz), are used to characterize the device speed.

Simulation: Numerical simulations of the optical profile and losses introduced by butt-coupling and the MMI coupler are performed using finite different eigenmode and 3D eigenmode expansion methods in Lumerical Software (2021). In order to determine the electrical properties of the PD in the depletion regime, we implemented electrical simulation with the Lumerical CHARGE solver. The work functions of Au and Ge are set to 5.1 and 4.5 eV, respectively. The Si substrate electron concentration was set to $2 \times 10^{19} \text{ cm}^{-3}$. From that, the map of free charge density in terms of holes and electrons in the SiGe epitaxial layer is interpolated in a 2D mesh configuration for the voltages from 0 to -8 V and then the total capacitance at different bias voltages can be estimated. By fitting between experimental and simulated data of $1/C^2$ as a function of bias voltages, the doping concentration in the epilayer can be extracted.

Supporting Information

Supporting Information is available from the Wiley Online Library or from the author.

Acknowledgements

This work was supported by ANR Light-up Project (ANR-19-CE24-0002-01). The fabrication of the device was partially performed at the Platform de Micro-NanoTechnologie/C2N, which is partially funded by the "Conseil Général de l'Essonne". This work was partly supported by the French RENATECH network. L-NESS laboratory is also acknowledged for SiGe epitaxial growth.

Conflict of Interest

The authors declare no conflict of interest.

Data Availability Statement

The data that support the findings of this study are available from the corresponding author upon reasonable request.

Keywords

germanium, integrated optics, mid-IR photonics, photodetection, silicon photonics

Received: August 18, 2022

Revised: October 20, 2022

Published online:

- [1] L. Huang, B. Dong, X. Guo, Y. Chang, N. Chen, X. Huang, W. Liao, C. Zhu, H. Wang, C. Lee, K.-W. Ang, *ACS Nano* **2019**, *13*, 913.
- [2] P.-L. Chen, Y. Chen, T.-Y. Chang, W.-Q. Li, J.-X. Li, S. Lee, Z. Fang, M. Li, A. Majumdar, C.-H. Liu, *ACS Appl. Mater. Interfaces* **2022**, *14*, 24856.

- [3] M. Montesinos-Ballester, L. Deniel, N. Koopmai, T. H. N. Nguyen, J. Frigerio, A. Ballabio, V. Falcone, X. Le Roux, C. Alonso-Ramos, L. Vivien, A. Bousseksou, G. Isella, D. Marris-Morini, *ACS Photonics* **2022**, *9*, 249.
- [4] Q. Huang, L. Zhong, J. Dong, O. Xu, Z. Zheng, T. Huang, J. Li, M. Xiang, S. Fu, Y. Qin, *Opt. Lett.* **2022**, *47*, 1478.
- [5] A. Gutierrez-Arroyo, E. Baudet, L. Bodiou, J. Lemaitre, I. Hardy, F. Faijan, B. Bureau, V. Nazabal, J. Charrier, *Opt. Express* **2016**, *24*, 23109.
- [6] Z. Han, V. Singh, D. Kita, C. Monmeyran, P. Becla, P. Su, J. Li, X. Huang, L. C. Kimerling, J. Hu, K. Richardson, D. T. H. Tan, A. Agarwal, *Appl. Phys. Lett.* **2016**, *109*, 071111.
- [7] B. Schwarz, P. Reininger, H. Detz, T. Zederbauer, A. M. Andrews, W. Schrenk, G. Strasser, *Sensors* **2013**, *13*, 2196.
- [8] W. Zhou, D. Wu, Q.-Y. Lu, S. Slivken, M. Razeghi, *Sci. Rep.* **2018**, *8*, 14866.
- [9] H. Lin, Z. Luo, T. Gu, L. C. Kimerling, K. Wada, A. Agarwal, J. Hu, *Nanophotonics* **2018**, *7*, 393.
- [10] M. Muneeb, A. Ruocco, A. Malik, S. Pathak, E. Ryckeboer, D. Sanchez, L. Cerutti, J. Rodriguez, E. Tournie, W. Bogaerts, M. Smit, G. Roelkens, *Opt. Express* **2014**, *22*, 27300.
- [11] A. Z. Subramanian, E. Ryckeboer, A. Dhakal, F. Peyskens, A. Malik, B. Kuyken, H. Zhao, S. Pathak, A. Ruocco, D. Groote, P. Wuytens, D. Martens, F. Leo, W. Xie, U. D. Dave, M. Muneeb, P. V. Dorpe, J. V. Campenhout, W. Bogaerts, P. Bienstman, N. L. Thomas, D. V. Thourhout, Z. Hens, G. Roelkens, R. Baets, *Photonics Res.* **2015**, *3*, B47.
- [12] M. Nedeljkovic, J. S. Penades, V. Mittal, G. S. Murugan, A. Z. Khokhar, C. Littlejohns, L. G. Carpenter, C. B. E. Gawith, J. S. Wilkinson, G. Z. Mashanovich, *Opt. Express* **2017**, *25*, 27431.
- [13] M. Montesinos-Ballester, V. Vakarin, Q. Liu, X. L. Roux, J. Frigerio, A. Ballabio, A. Barzaghi, C. Alonso-Ramos, L. Vivien, G. Isella, D. Marris-Morini, *Opt. Express* **2020**, *28*, 12771.
- [14] M. Montesinos-Ballester, C. Lafforgue, J. Frigerio, A. Ballabio, V. Vakarin, Q. Liu, J. M. Ramirez, X. Le Roux, D. Bouville, A. Barzaghi, C. Alonso-Ramos, L. Vivien, G. Isella, D. Marris-Morini, *ACS Photonics* **2020**, *7*, 3423.
- [15] S. Keuleyan, E. Lhuillier, V. Brajuskovic, G.-S. Philippe, *Nat. Photonics* **2011**, *5*, 489.
- [16] E. Guglielmi, P. Su, F. Zanetto, K. Stoll, S. Serna, G. Ferrari, M. Sampietro, K. Wada, L. C. Kimerling, A. Agarwal, *J. Light. Technol.* **2021**, *39*, 7326.
- [17] D. Palaferri, Y. Todorov, A. Bigioli, A. Mottaghizadeh, D. Gacemi, A. Calabrese, A. Vasanelli, L. Li, A. G. Davies, E. H. Linfield, F. Kapsalidis, M. Beck, J. Faist, C. Sirtori, *Nature* **2018**, *556*, 85.
- [18] M. Hakl, Q. Lin, S. Lepillet, M. Billet, J.-F. Lampin, S. Pirotta, R. Colombelli, W. Wan, J. C. Cao, H. Li, E. Peytavit, S. Barbieri, *ACS Photonics* **2021**, *8*, 464.
- [19] J. Hillbrand, L. M. Krüger, S. D. Cin, H. Knötig, J. Heidrich, A. M. Andrews, G. Strasser, U. Keller, B. Schwarz, *Opt. Express* **2021**, *29*, 5774.
- [20] V. Vakarin, J. Ramirez, J. Frigerio, A. Ballabio, X. Le Roux, Q. Liu, D. Bouville, L. Vivien, G. Isella, D. Marris-Morini, *Opt. Lett.* **2017**, *42*, 3482.
- [21] X. Zhou, D. Yang, D. Ma, *Adv. Opt. Mater.* **2015**, *3*, 1570.
- [22] B. Zheng, H. Zhao, B. Cerjan, S. Yazdi, E. Ringe, P. Nordlander, N. J. Halas, *Appl. Phys. Lett.* **2018**, *113*, 101105.
- [23] M. Grajower, B. Desiatov, N. Mazurski, J. Shappir, J. B. Khurgin, U. Levy, *ACS Photonics* **2017**, *4*, 1015.
- [24] M. Tanzid, A. Ahmadvand, R. Zhang, B. Cerjan, A. Sobhani, S. Yazdi, P. Nordlander, N. J. Halas, *ACS Photonics* **2018**, *5*, 3472.
- [25] R. R. Grote, B. Souhan, N. Ophir, J. B. Driscoll, K. Bergman, H. Bahkru, W. M. J. Green, R. M. Osgood, *Optica* **2014**, *1*, 264.
- [26] J. Ackert, D. Thomson, L. Shen, A. Peacock, P. Jessop, G. Reed, G. Mashanovich, A. Knights, *Nat. Photonics* **2015**, *9*, 393.
- [27] W. Barth, K. Elsaesser, W. Güth, *Phys. Status Solidi A* **1976**, *34*, 153.
- [28] E. A. Fitzgerald, Y. Xie, D. Monroe, P. J. Silverman, J. M. Kuo, A. R. Kortan, F. A. Thiel, B. E. Weir, *J. Vac. Sci. Technol., B* **1992**, *10*, 1807.
- [29] C. Rosenblad, H. R. Deller, A. Dommann, T. Meyer, P. Schroeter, H. von Känel, *J. Vac. Sci. Technol., A* **1998**, *16*, 2785.